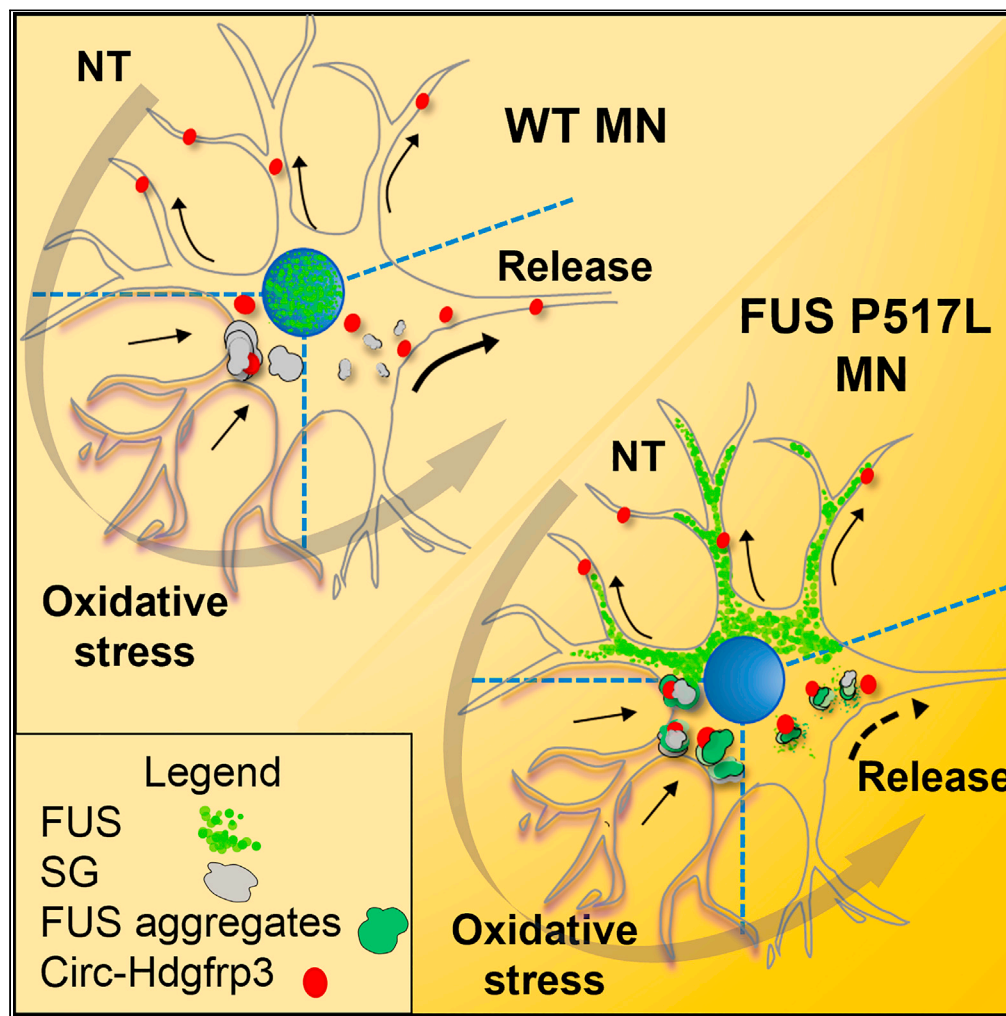**Article**

Circ-Hdgfrp3 shuttles along neurites and is trapped in aggregates formed by ALS-associated mutant FUS

Eleonora D'Ambra, Tiziana Santini, Erika Vitiello, Sara D'Uva, Valentina Silenzi, Mariangela Morlando, Irene Bozzoni

irene.bozzoni@uniroma1.it (I.B.)
mariangela.morlando@unipg.it (M.M.)

Highlights

Circ-Hdgfrp3 is detected in MN neurites through a highly sensitive *in situ* approach

Oxidative stress exacerbates circ-Hdgfrp3 entrapment in cytoplasmic granules

FUS P517L-positive aggregates release circ-Hdgfrp3 less efficiently than WT SGs

Human circ-Hdgfrp3 associates with aggregates containing ALS-related FUS P525L

Article

Circ-Hdgfrp3 shuttles along neurites and is trapped in aggregates formed by ALS-associated mutant FUS

Eleonora D'Ambra,[1,2,5] Tiziana Santini,[1,2,5] Erika Vitiello,[1,3] Sara D'Uva,[1] Valentina Silenzi,[1,2] Mariangela Morlando,[4,*] and Irene Bozzoni[1,2,3,6,*]

SUMMARY

CircRNAs belong to a family of RNA molecules which are conserved in evolution, have tissue-specific expression, and are abundant in neuronal cells. Here, we define several features of circ-Hdgfrp3 and describe interesting alterations occurring in motor neurons (MNs) carrying ALS-associated FUS mutations. Through a highly sensitive *in situ* approach we describe that circ-Hdgfrp3 traffics along neurites, while upon oxidative stress it is retained in the perinuclear region. While in wild-type stressed MNs, circ-Hdgfrp3 localizes in stress granules (SGs), in MNs carrying mutant FUS, a higher proportion of circ-Hdgfrp3 was trapped into cytoplasmic aggregates. Upon stress removal, circ-Hdgfrp3 was easily freed from SGs whereas it was less efficiently released from FUS-aggregates. We found that the human circ-Hdgfrp3 counterpart was also similarly associated to mutant FUS-aggregates in stressed neuronal cells. Overall, the alteration of circ-Hdgfrp3 trafficking adds a further layer of complexity to the role of FUS-aggregates in ALS disease.

INTRODUCTION

CircRNAs belong to a class of covalently closed circular RNA molecules arising from a non-canonical splicing event in which a downstream 5′ splice site (SS) is joined to an upstream 3′ SS. Such a reaction produces a novel splice junction, named back-splicing junction (BSJ) (Wilusz, 2018), which represents a distinctive feature of circRNAs and allows them to be discriminated from their corresponding linear counterparts (Salzman et al., 2012; Memczak et al., 2013). Indeed, high-throughput RNA sequencing methodologies that recognize reads mapping on the back-splicing junction (BSJ) (Mortazavi et al., 2008) have enabled the identification of a prominent number of circRNAs differentially expressed in tissues, during development and in different pathological conditions (Salzman et al., 2012; Memczak et al., 2013; Rybak-Wolf et al., 2014; Veno et al., 2015; Chen et al., 2019; Mahmoudi and Cairns, 2019; Salvatori et al., 2020). CircRNAs also show a high degree of conservation among species (Jeck et al., 2013; Wang et al., 2014; Westholm et al., 2014). Different functional roles have been assigned to circRNAs (D'Ambra et al., 2019): the majority of them have the ability to bind microRNAs, thus acting as regulators of their activity on target messenger RNAs (mRNAs) (Hansen et al., 2013; Piwecka et al., 2017). CircRNAs can also regulate protein levels and activity (Ashwal-Fluss et al., 2014; Liu et al., 2019; Rossi et al., 2019), they can be substrates for translation (Legnini et al., 2017; Pamudurti et al., 2017) and can also regulate transcription of their host gene (Li et al., 2015). Notably, circRNAs have been shown to be highly enriched in the brain, where they are also capable of reaching the synapses (Rybak-Wolf et al., 2014; Ashwal-Fluss et al., 2014; You et al., 2015), be embedded in extracellular vesicles (Lasda and Parker, 2016), including exosomes (Fanale et al., 2018), and be secreted in cerebrospinal fluid (Hosaka et al., 2019). The relevance of circRNAs in the neuronal system is further supported by experimental evidence demonstrating that these molecules are altered in neurological conditions (Lukiw, 2013; Errichelli et al., 2017; Wang et al., 2018), and that their expression and trafficking through synapses can be modulated by neuronal stimuli (You et al., 2015). In a previous work, we demonstrated that a set of circRNAs expressed in murine motoneurons (MNs) are affected by the depletion of FUS (Errichelli et al., 2017), which is an ubiquitous RNA binding protein involved in different steps of DNA/RNA metabolism, particularly in splicing (Lagier-Tourenne et al., 2010).

Mutations of the FUS gene are related to the familial form of Amyotrophic Lateral Sclerosis (fALS) (Kwiatkowski et al., 2009; Vance et al., 2009), a neurodegenerative disease characterized by the degeneration of

[1]Department of Biology and Biotechnology 'Charles Darwin', Sapienza University of Rome, Rome, Italy

[2]Center for Life Nano- & Neuro-Science, Fondazione Istituto Italiano di Tecnologia, Rome, Italy

[3]Center for Human Technology@ Istituto Italiano di Tecnologia, Genova, Italy

[4]Department of Pharmaceutical Sciences, "Department of Excellence 2018-2022", University of Perugia, Perugia, Italy

[5]These authors contributed equally

[6]Lead contact

*Correspondence:
irene.bozzoni@uniroma1.it (I.B.),
mariangela.morlando@unipg.it (M.M.)

https://doi.org/10.1016/j.isci.2021.103504

upper and lower MNs leading to muscular weakness and atrophy, and death due to respiratory failure, 3–5 years post symptom onset (Taylor et al., 2016). Notably, although a small percentage of patients with fALS carry FUS mutations (Kwiatkowski et al., 2009; Vance et al., 2009), this protein together with TDP-43 links ALS to Frontotemporal Lobar Degeneration because in both pathologies these proteins have been found to form insoluble cytosolic inclusions (Neumann et al., 2009; Dormann and Haass, 2011). The FUS protein is mainly nuclear; instead different mutant derivatives delocalize to the cytoplasm where, upon different insults, they form insoluble aggregates which sequester several types of RNAs and proteins (Dormann et al., 2010; Bosco et al., 2010; Lenzi et al., 2015). Moreover, axonal transport abnormalities have also been reported in in vitro-derived FUS mutant MNs and in ALS animal models (Williamson and Cleveland, 1999; Baldwin et al., 2016; Guo et al., 2017; Sama et al., 2017). This might affect the transport from the cell body to the axon periphery of organelles, vesicles, proteins, mRNPs (messenger RiboNucleoProteins), and lipids that are normally required for correct synaptic function (De Vos and Hafezparast., 2017). As several circRNAs also show synaptic localization (You et al., 2015), in particular during synaptic plasticity, we investigated circRNA localization in murine MNs carrying the FUS-P517L mutation, corresponding to the human FUS-P525L, which is linked to one of the most severe and juvenile forms of fALS (Chiò et al., 2009; Conte et al., 2012).

Among the circRNAs previously identified as expressed in MNs and modulated by the FUS protein, we selected circ-Hdgfrp3 (previously named c-31 in Errichelli et al., 2017), a multi-exonic circRNA that arises from the Hdgfrp3 gene. This choice was mainly dictated by the fact that circ-Hdgfrp3 is strongly upregulated during in vitro MN differentiation of mouse embryonic stem cells (mESCs), accumulates at high levels in mature MNs, and is conserved in humans (Errichelli et al., 2017). Moreover, its host gene has been described as a neurotrophic and neuroprotective factor, as well as being involved in neuritogenesis (El-Tahir et al., 2009; Abouzied et al., 2010).

In this study, using a new sensitive single-molecule FISH technology (Basescope), we found that both in wild type (WT) and mutant FUS MNs, a considerable fraction of circ-Hdgfrp3 localizes in neurites. Upon oxidative stress, the circRNA became retained in SGs and in FUS-aggregates, lacking almost completely at the cell periphery. Neurite localization of circ-Hdgfrp3 was recovered after stress removal, even if in FUS-P517L aggregates the release of the circRNA was slightly slower compared to its release from SGs. Association to FUS-aggregates was also found in neuronal cells carrying the corresponding highly pathogenic human mutation FUS-P525L. In conclusion, our work identifies a novel type of non-coding RNA which is sequestered within FUS-aggregates and, as a consequence of this, becomes mislocalized.

RESULTS

In situ analysis of circ-Hdgfrp3

This study focuses on circ-Hdgfrp3, a conserved multi-exonic circRNA arising from exons 2–5 of the Hdgfrp3 gene (Figure 1A). This circRNA resulted strongly upregulated during in vitro MN differentiation of mESCs and accumulated at high levels in mature MNs (Errichelli et al., 2017). In order to gain insight about circ-Hdgfrp3 function, we decided to investigate its subcellular localization through an imaging approach. A new single-molecule FISH technology called Basescope was applied to MNs derived from mESCs induced to differentiate toward the MN-specific fate, according to Wichterle and Peljto (2008). Following this protocol, embryoid bodies (EBs) are formed after 6 days of differentiation. EBs are then dissociated and plated as a mixed cell population in the presence of BDNF, GDNF, and CNTF to induce MN maturation and axon elongation (Wu et al., 2012) (Figure S1A). The mixed population contains approximately ≈50% of *bona fide* MNs, as indicated by the expression of the GFP reporter gene under the control of the MN-specific Hb9 promoter and by the parallel onset of the MN-specific marker ISLET (Figures S1B–S1D). Owing to this enrichment, the mixed neuronal population, without discriminating for GFP positive or negative cells, was used for all the analyses. The Basescope technology is based on the use of two Z-probes that allow the formation of a signal amplification "tree" only when bound to adjacent sequences. This technology, previously used to successfully identify splice variants (Erben et al., 2018; Guo et al., 2018), was applied to circ-Hdgfrp3 by designing two Z-probes complementary to the sequences flanking the BSJ, thus avoiding cross hybridization with the linear mRNA counterpart (Figure 1B). Two days after EBs dissociation, the cells were fixed with 4% paraformaldehyde and analyzed through the Basescope procedure in combination with ISLET immunofluorescence to identify the MN-specific cell population (Figure S1B). Clear hybridization signals were obtained with circ-Hdgfrp3-specific probes (Figures 1C and S1E), which were almost exclusively present in MN cells, expressing both GFP and ISLET, whereas a small percentage was present in non-MN cells,
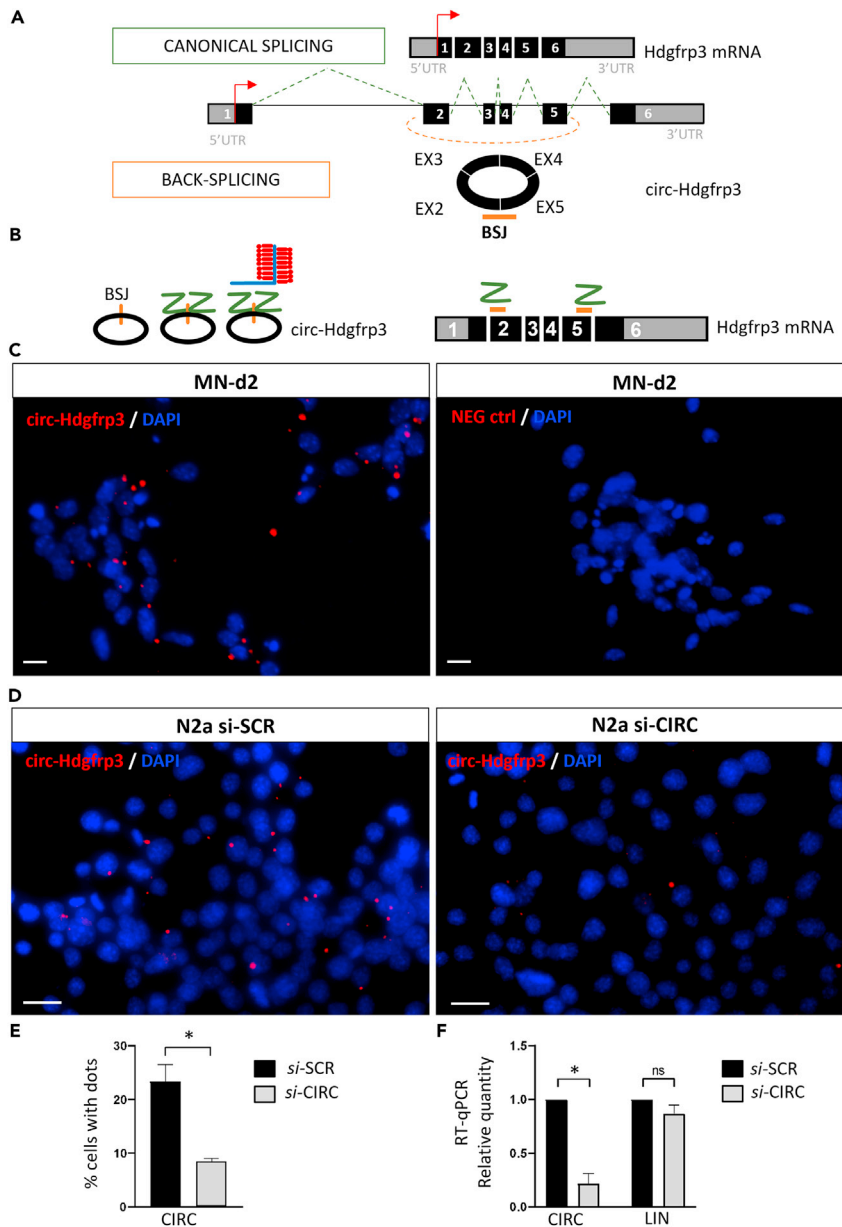
Figure 1. *In situ* detection of circ-Hdgfrp3

(A) Schematic representation of Hdgfrp3 pre-mRNA, mRNA, and circ-Hdgfrp3. Canonical and back-splicing events are also indicated. Exonic and intronic regions are depicted by boxes (gray boxes for 5'- and -3''- UTR and black boxes for the coding region) and lines respectively.

(B) Schematic representation of Basescope-FISH technology used for circ-Hdgfrp3 detection (left). Two Z-probes targeting the single BSJ, absent in Hdgfrp3 mRNA (right), together with the amplification "tree" are shown.

(C) Basescope-FISH for circ-Hdgfrp3 (left panel) and for the bacterial RNA DapB (NEG ctrl, right panel) performed on MNs at day 2 after dissociation (20× magnification).

(D) Basescope-FISH for circ-Hdgfrp3 performed on N2a cells transfected with siRNAs scramble (si-SCR; left panel) and siRNAs against the BSJ of circ-Hdgfrp3 (si-CIRC; right panel) (40× magnification).

(E) Graph showing the quantification of circ-Hdgfrp3 dots (shown in panels "d") in N2a cells upon si-SCR and si-CIRC treatments. Error bars represent SEM (N = 3); approximately a total of 1000 cells have been considered for each replicate on images acquired with 10× magnification.

Figure 1. *Continued*
(F) Graph showing the RT-qPCR relative quantity of circ-Hdgfrp3 (CIRC) and of its linear counterpart (LIN) in N2a cells upon si-SCR and si-CIRC treatments (panels in "d"). Values were normalized against ATP5O and expressed as relative quantities with respect to si-SCR set to a value of 1. Error bars represent ±SEM (N = 3). *p < 0.05 and ns (not significant; p > 0.05) correspond to an unpaired two-tailed Student's t test. All scale bars correspond to 10 μm.

negative for both MN markers (Figures S1B, S1C, and S1F). The specificity of the circ-Hdgfrp3 hybridization was assessed using two Z-probes designed for the bacterial RNA DapB as a negative control, which did not reveal any signal (Figures 1C and S1E, NEG ctrl). A further control for the specificity of the FISH approach was made in murine N2a cells that are easily transfectable even if expressing circ-Hdgfrp3 at lower levels (Figure S1G). These cells were treated with siRNAs against the circ-Hdgfrp3 BSJ producing a strong and significant reduction of circ-Hdgfrp3 positive cells (Figures 1D and 1E). Under these conditions, we observed a specific downregulation of the circRNA, while the levels of the linear counterpart remained unaffected (Figure 1F). Altogether, these results indicate that the Basescope methodology provides an effective and specific method for circRNA detection. We also noticed that this methodology produces dots of different sizes; this could be due to either the presence of a different number of circRNA molecules in the same district or to an intrinsic limitation of the technology that, being based on exponential probe amplification, does not allow refined quantifications.

In order to study the subcellular distribution of circ-Hdgfrp3, we combined the Basescope procedure with immunofluorescence for TUBB3. Figures 2A and S2A show that circ-Hdgfrp3 is localized in cell bodies and in neurites of MNs suggesting that this molecule can reach the cellular periphery.

We then tested whether circ-Hdgfrp3 localization in neurites paralleled MN maturation. We performed Basescope-FISH assays for circ-Hdgfrp3 at different time points (Figure 2A). Notably, we observed a significant increase in the number of circ-Hdgfrp3 signals in neuronal processes during maturation, paralleling the formation of a dense network of neurites (Figures 2B and S2B). These results indicate that the establishment of neuronal connections and the increased branching correlate well with the localization of circ-Hgfrp3 in neurites, suggesting a possible role of this molecule at the periphery of MNs.

Circ-Hdgfrp3 localization is altered in stress conditions

Circ-Hdgfrp3 biogenesis was previously shown to be affected by FUS depletion (Errichelli et al., 2017), while it is not altered in MNs carrying the P517L knockin FUS mutation in homozygosity (Capauto et al., 2018). The FUS-P517L mutation corresponds to the human FUS-P525L, which is linked to a severe and juvenile form of fALS (Chiò et al., 2009; Conte et al., 2012). Because this mutation is known to cause a strong cytoplasmic delocalization of FUS (Lenzi et al., 2015), we asked whether this might influence circ-Hdgfrp3 localization.

In order to test this hypothesis, we performed Basescope-FISH for circ-Hdgfrp3 combined with immunofluorescence for TUBB3 and FUS in WT and FUS-P517L MNs. In mutant MNs, we did not observe any change in circ-Hdgfrp3 localization with respect to the WT condition: the circRNA was still present both in the soma and in neurites (Figure 3A upper panels). This result indicates that the FUS mutation does not affect circ-Hdgfrp3 localization.

Mutant FUS is known to form cytoplasmic aggregates in MNs and glia from postmortem tissues (Kwiatkowski et al., 2009; Vance et al., 2009) and this can be recapitulated *in vitro* by applying different types of cellular stress (Lenzi et al., 2015). Therefore, we treated WT and mutant MNs with sodium arsenite (ARS), and we noticed that oxidative stress compromised circ-Hdgfrp3 localization in neurites, both in WT and FUS mutant cells. Indeed, we observed a significant retention of circ-Hdgfrp3 in the soma and perinuclear regions with an almost complete absence at the periphery (Figures 3A lower panels and 3B). Notably, this was not due to a disruption of the cytoskeleton (Zhou et al., 1999; Gardiner et al., 2013) because in our experimental conditions the neuronal processes labeled with TUBB3 antibodies remained intact (Figure 3A).

Circ-Hdgfrp3 associates to different types of granules

As oxidative stress induces SG formation, we hypothesized that the retention of circ-Hdgfrp3 in the perinuclear region could be due to a possible recruitment of the circRNA in these granules.
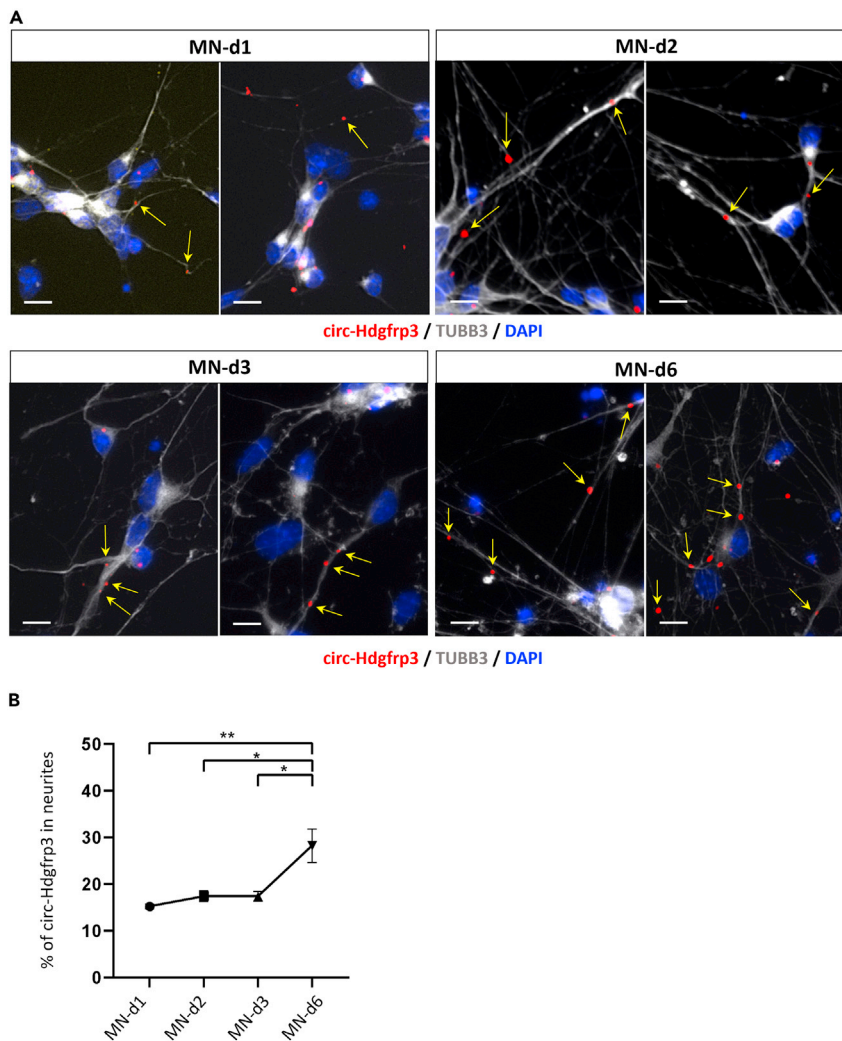
Figure 2. Localization of circ-Hdgfrp3 in neurites of MNs

(A) Basescope-FISH for circ-Hdgfrp3 (red) and Immunofluorescence for TUBB3 (white) in MNs at different time points of maturation (d1, d2, d3, and d6;(20× magnification). Yellow arrows point to circ-Hdgfrp3 in neurites.

(B) Graph showing the percentage of circ-Hdgfrp3 molecules detected in neuronal processes at different time points of MN maturation. Error bars represent ±SEM (N = 4). Approximately 150 cells have been analyzed for each replicate. *p < 0.05 and **p < 0.01 correspond to ordinary one-way Anova multiply comparison. All scale bars correspond to 10 μm.

We performed circ-Hdgfrp3 Basescope-FISH in ARS-treated MNs, coupled with immunofluorescence for FUS and TIAR (TIA-1 related protein), the latter being selected as a canonical marker of SGs (Kedersha et al., 1999) (Figures 4A and S3).

The presence of circ-Hdgfrp3 in granules was then quantified in WT and in FUS-P517L MNs. This was defined by 3D rendering and by the coplanarity of circ-Hdgfrp3 signals with those of FUS or TIAR along the z axis (Figures 4B, S4A, and S4B). By applying these procedures, we observed that in WT MNs only 10% of circ-Hdgfrp3 was associated with TIAR-positive SGs. On the contrary, in FUS-P517L MNs, 16% of circ-Hdgfrp3 was found associated with TIAR and FUS in SGs, while an additional 18% was found associated with FUS-aggregates devoid of the SG marker TIAR (Figure 4C).

Although mutant FUS mostly colocalize with stress granule markers (Bosco et al., 2010; Lenzi et al., 2015), we could detect some FUS assemblies that do not overlap with TIAR in our system. We will refer to these as FUS-aggregates in order to distinguish them from granules containing both TIAR and FUS.
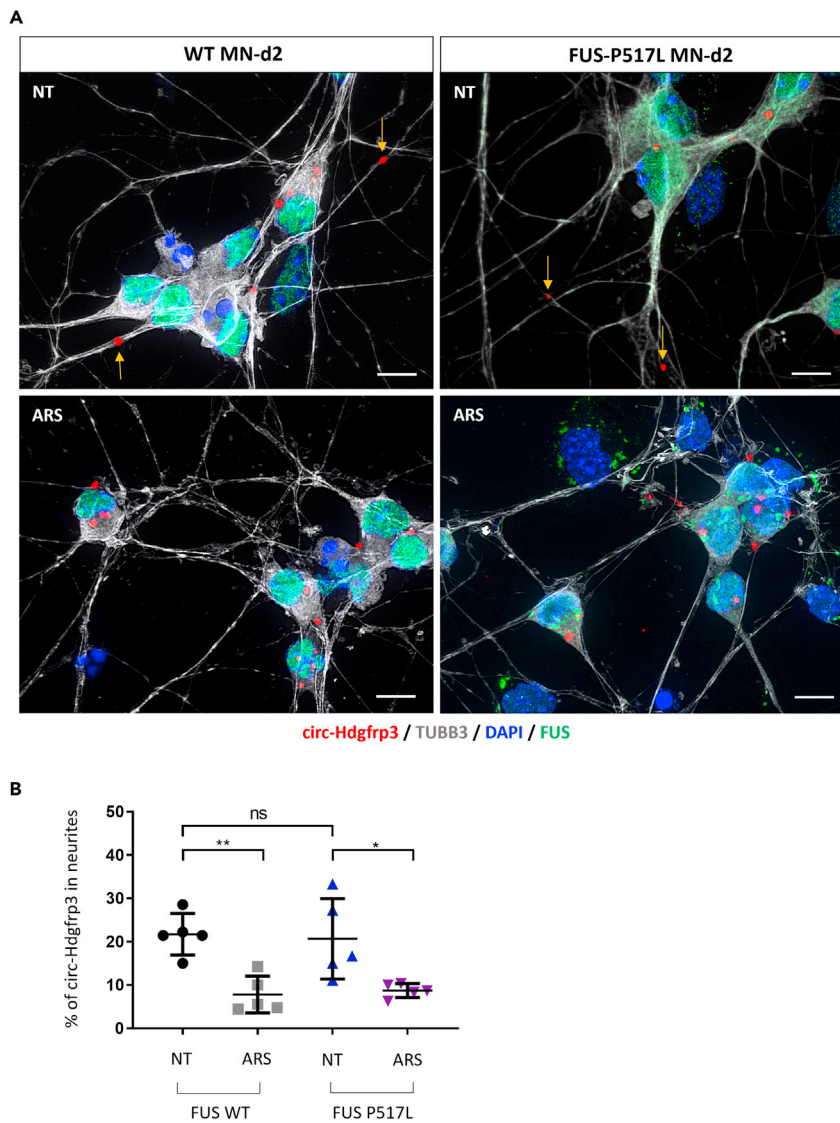
Figure 3. Circ-Hdgfrp3 localization in stress conditions

(A) Basescope-FISH for circ-Hdgfrp3 (red) and Immunofluorescence for TUBB3 (white) and FUS (green) in WT and FUS-P517L MNs untreated (NT, upper panels) and treated with arsenite 0.5 mM for 1 h (ARS, lower panels). Arrows indicate circ-Hdgfrp3 signals localized in neuronal processes (60× magnification).

(B) Scatterplot showing the percentage of circ-Hdgfrp3 signals in neuronal processes in WT and FUS-P517L MNs treated as in "a".Error bars represent ±SD of 5 groups of 20 cells. *p < 0.05, **p < 0.01, and ns (not significant; p > 0.05) correspond to an unpaired two-tailed Student's t test. All scale bars correspond to 10 μm.

We then focused on FUS-containing SGs and through the signal distribution analysis of TIAR and FUS with respect to circ-Hdgfrp3, we observed that TIAR overlapped with circ-Hdgfrp3 in one-third of them (Figures S4A and S4C), whereas FUS was found in intimate association with the circRNA in 63% of the cases (Figure S4B upper panels and S4C). Whether these differences reflect different types of assemblies or dynamic processes of SG modification is difficult to assess. Instead, a tight interconnection between circ-Hdgfrp3 and FUS seemed to be common in FUS-aggregates independent from SGs (Figure S4B lower panels).

We also tested the level of colocalization between circ-Hdgfrp3 and the cytoplasmic FUS-P517L protein in untreated versus ARS conditions and found that a significant overlap was detectable only in stress
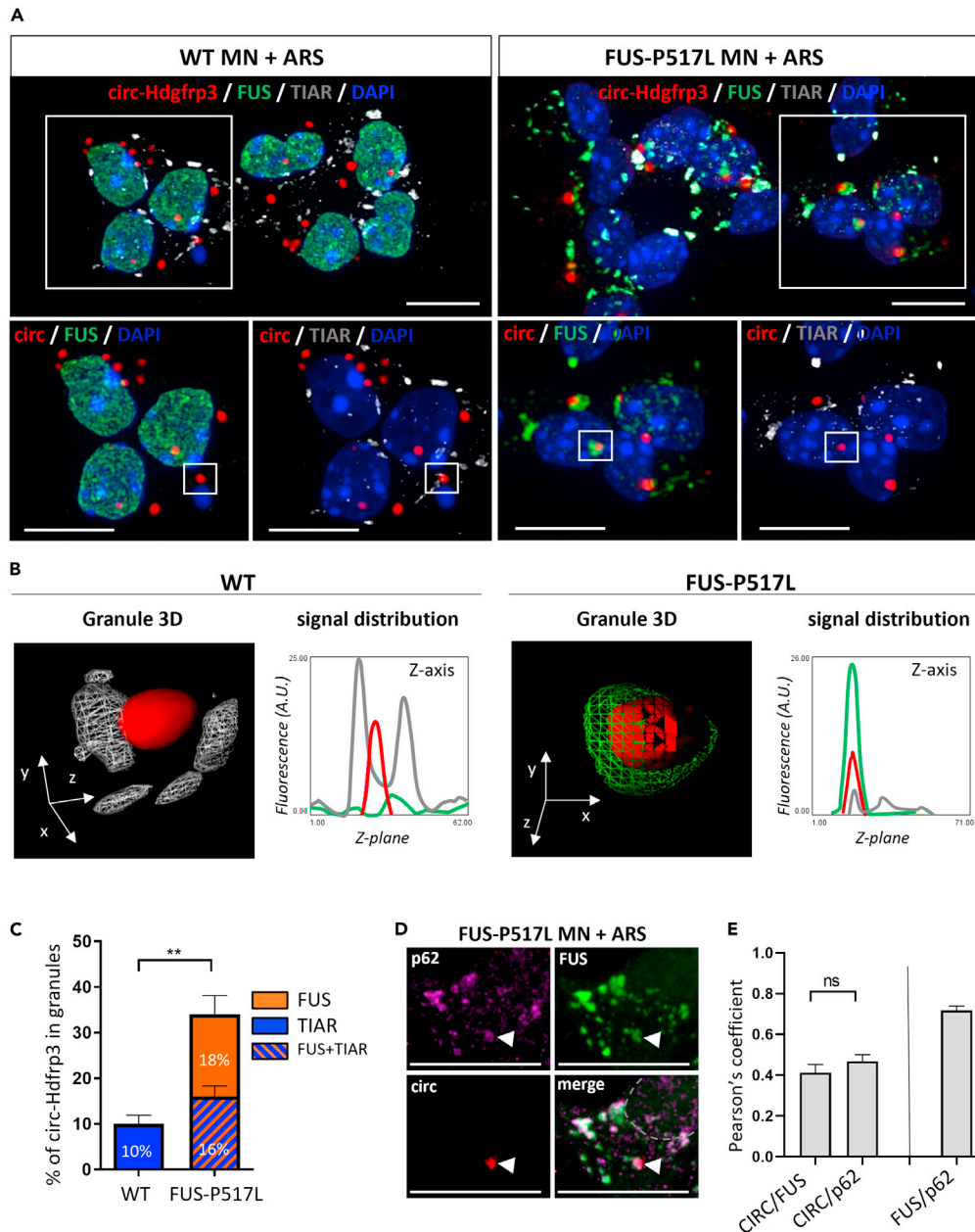
Figure 4. Spatial characterization of granules colocalizing with circ-Hdgfrp3

(A) Upper panels: Basescope-FISH for circ-Hdgfrp3 (red) and Immunofluorescence for FUS (green) and TIAR (white) in WT and FUS-P517L MNs treated with arsenite (ARS) (60× magnification). Lower panels: digital magnifications of white boxes with FUS (left) and TIAR (right) separate channels.

(B) 3D rendering showing architecture of the granules (shown in white boxes, lower magnification of panel a) along the x, y, and z axes and graph showing the distributions of circ-Hdgfrp3 (red), FUS (green), and TIAR (gray) fluorescence intensity (A.U.= Arbitrary Units) along the Z axes. Left: WT granule; right: FUS-P517L granule.

(C) Graph showing the percentage of circ-Hdgfrp3 dots contained in TIAR and/or FUS granules in WT and in FUS-P517L MNs. Error bars represent ±SEM (N = 3).

(D) Immunofluorescence for p62/SQSTM1 (p62, magenta), FUS (green), and Basescope-FISH for circ-Hdgfrp3 (red) in FUS-P517L MNs treated with arsenite (ARS) (60× magnification). White arrows show circ-Hdgfrp3 colocalizing with p62 and FUS.

(E) Histogram shows the average of 3D-Pearson's correlation coefficients for circ-Hdgfrp3 and FUS (CIRC/FUS), circ-Hdgfrp3 and p62 (CIRC/p62), FUS and p62 (FUS/p62). ns (not significant; $p > 0.05$) and $**p < 0.01$ correspond to an unpaired two-tailed Student's t test. (N = 18 granules). All scale bars correspond to 10 μm.

conditions (Figures S5A and S5B, left panels). This observation was highlighted by 3D rendering and ImageJ z axis plot profile (Figures S5A and S5B, middle and right panels) and quantified by 3D Pearson's correlation coefficient (r-values; Figures S5C and S5D) which indicates colocalization if r>0 and non-colocalization if r<0. Notably, the circ-Hdgfrp3/FUS-P517L colocalization in ARS-treated cells was significantly higher with respect to untreated conditions (Figures S5C, r>0 average), further demonstrating the intimate proximity of the two factors in stressed cells and reinforcing the coplanarity analysis provided on Z-stacks (Figures S5A and S5B). In addition, the distribution of r-values for the untreated and ARS conditions showed opposite trends, with the tendency to be lower than "0" for the former and higher than "0" for the latter (Figure S3H).

We also tested the presence of two different aggregate markers, p62/SQSTM1 and ubiquitin (Lagier-Tourenne et al., 2010), in FUS-aggregates containing circ-Hdgfrp3 (Figures 4D and S6 upper panel). We observed that p62 signals colocalized with FUS-aggregates with or without circ-Hdgfrp3. We more accurately analyzed the colocalization of circ-Hdgfrp3 signals with FUS or p62 through 3D Pearson's correlation; the data show a positive correlation coefficient in both cases (r>0; Figure 4E). Through the same analysis, we found that the overlap between FUS and p62 had an even higher correlation coefficient (Figure 4E). In the case of ubiquitin, antibodies specific for both the free and conjugated forms revealed that upon stress it is present in assemblies that do not overlap with FUS-aggregates (Figure S6). This result is in line with previous observations, showing that FUS-aggregates analyzed *in vitro* do not always colocalize with ubiquitin (Farrawell et al., 2015).

Finally, we performed a staining for TDP-43, an RNA binding protein sharing many common features with FUS (Lagier-Tourenne et al., 2010), in order to verify whether it colocalizes with FUS-aggregates containing circ-Hdgfrp3. In the brain and spinal cord of patients with ALS, FUS-aggregates have been shown to lack TDP-43 (Lagier-Tourenne et al., 2010; Blair et al., 2010). Indeed, we did not observe any colocalization of TDP-43 with cytoplasmic FUS-aggregates, regardless of whether these contained circ-Hdgfrp3 (Figure S6 lower panel).

We then evaluated the re-localization of circ-Hdgfrp3 in neurites upon stress removal and tested the ability of SGs and FUS-positive granules to dissolve and release circ-Hdgfrp3 (Figures 5A–5D). We found that after 240 min, WT MNs recovered almost 64% of circ-Hdgfrp3 localization in neurites, whereas mutant MNs showed a slightly lower (51%), although significant, release at the periphery (Figure 5B). Moreover, with respect to the SGs formed in the WT condition, cytoplasmic assemblies in mutant MNs displayed a significantly higher retention of the circRNA upon stress removal (Figures 5C and 5D).

Altogether, these results indicate that mutant FUS exacerbates the effect of oxidative stress in sequestering circ-Hdgfrp3 in cytoplasmic assemblies. Because SGs can be dissolved more efficiently than FUS-containing aggregates upon stress removal, it can be hypothesized that the long-lasting trapping of circ-Hdgfrp3 inside FUS inclusions in ALS-related conditions might interfere with its trafficking and possibly with its functional activity.

Circ-Hdgfrp3 associates to FUS-aggregates in human neuronal cells

We then analyzed the localization of circ-Hdgfrp3 in SK-N-BE cells expressing circ-Hdgfrp3 together with either the WT FUS or the FUS-P525L mutant. The results indicate that also in these cells, circ-Hdgfrp3 is localized in the neurites in untreated conditions (Figure 6A); whereas, upon ARS treatment, it associates with SGs in WT cells (17%) and even more with mutant FUS-positive aggregates (45%), indicating that this feature is conserved between mouse and human (Figures 6B–6D). As a control, upon stress induction the more ubiquitous circ-ZNF609 (Legnini et al., 2017) did not show any change in the association with SGs or FUS-aggregates in WT vs mutant condition (Figures S7A and S7B).

DISCUSSION

CircRNA detection methods are quite challenging because these molecules share their sequences with the corresponding linear mRNA apart from the single region where the back-splicing reaction occurs. Therefore, methods that use multiple probes, while on one hand reach high levels of sensitivity, on the other they do not allow the distinction between the circular molecule and its linear counterpart (Orjalo and Johansson, 2016; Kocks et al., 2018). To overcome this limit, we applied a new FISH technology, Basescope, which makes use of two Z-probes to target the region spanning across the BSJ, which are then amplified by a
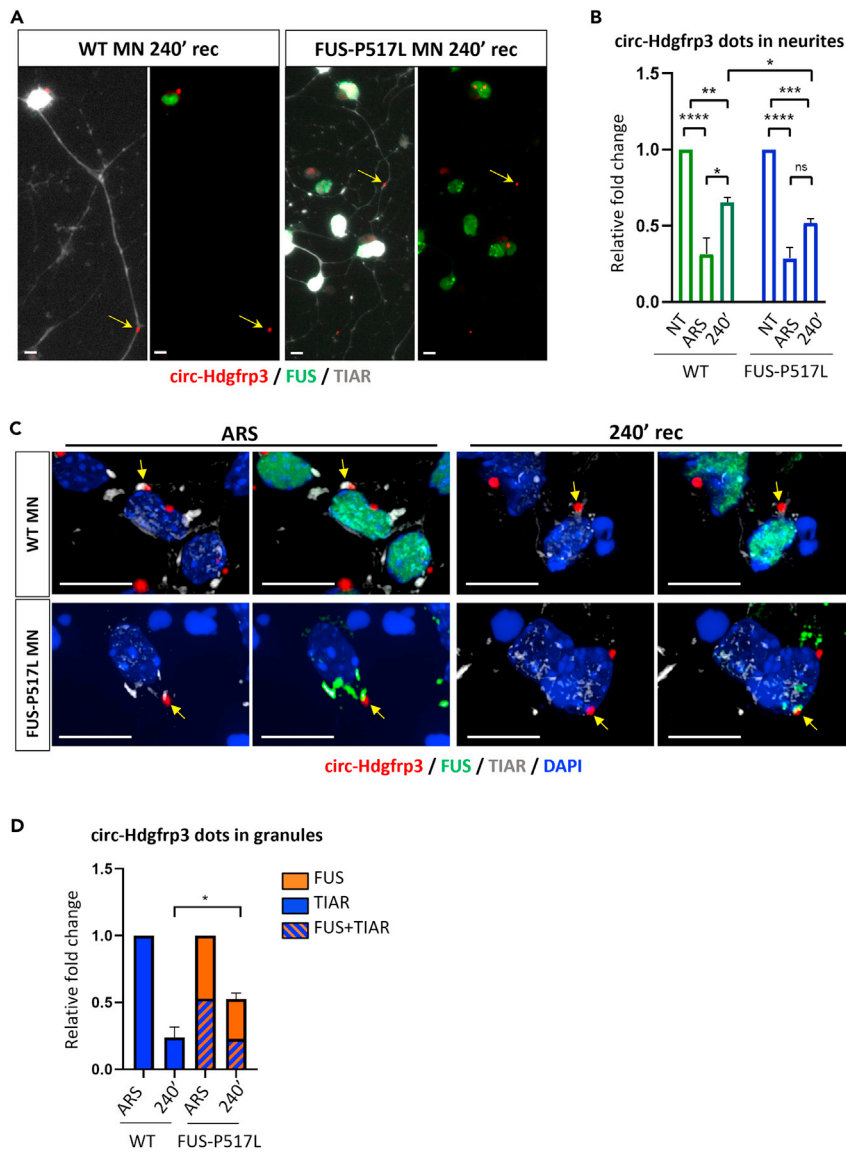
Figure 5. Upon stress removal circ-Hdgfrp3 partially recovers its neurites localization and shows higher persistence in FUS-aggregates with respect to SGs

(A) Basescope-FISH for circ-Hdgfrp3 (red) and Immunofluorescence for FUS (green) and TIAR (white) in WT and FUS-P517L MNs upon stress removal (240 min of recovery: 240' rec). Arrows indicate circ-Hdgfrp3 in neurites (20× magnification).

(B) Graph showing the fraction of circ-Hdgfrp3 in neurites in arsenite (ARS) condition and after 240 min of stress removal (240'), expressed as relative fold change respect to non-treated condition (NT) set to a value of 1. Error bars represent ±SEM (N = 3), approximately 200 circ-Hdgfrp3 spots have been counted for each replicate.

(C) Basescope-FISH for circ-Hdgfrp3 (red) and Immunofluorescence for FUS (green) and TIAR (white) in WT and FUS-P517L MNs treated with arsenite and upon stress removal (240' rec). Arrows indicate circ-Hdgfrp3 in TIAR and/or FUS positive granules. Acquisitions with 100× magnification.

(D) Graph showing the fraction of circ-Hdgfrp3 retained in granules (TIAR and/or FUS positive), in WT and FUS-P517L MNs, after 240 min of stress removal (240'), expressed as relative fold change respect to arsenite condition (ARS) set to a value of 1. Error bars represent ±SEM (N = 4). Approximately 60 circ-Hdgfrp3 spots have been analyzed for each condition.

*p < 0.05, **p < 0.01, ***p < 0.001, ****p < 0.0001, and ns (not significant; p > 0.05) correspond to one-way ANOVA test (graph b) and an unpaired two-tailed Student's t test (graph d). All scale bars correspond to 10 μm.
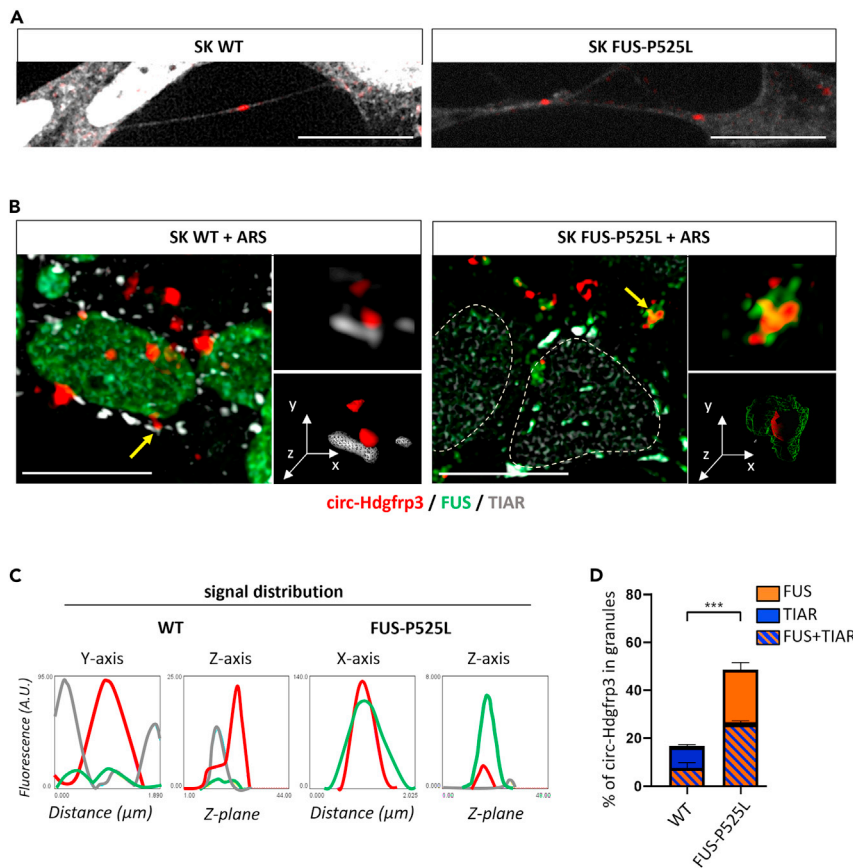
Figure 6. Circ-Hdgfrp3 localization in human neuronal cells

(A) Human circ-Hdgfrp3 spots (red) by Basescope-FISH in neuronal processes viewed by Immunofluorescence for TIAR (white signal) in human SK-N-BE cells expressing WT and FUS-P525L at day 6 of differentiation.

(B) Basescope-FISH for human circ-Hdgfrp3 (red) and Immunofluorescence for FUS (green) and TIAR (white) in SK-N-BE cells. Digital magnifications of the granules are shown at the side of each panel.

(C) Graphs showing the distributions of human circ-Hdgfrp3 (red), TIAR (gray), and FUS (green) fluorescence intensity (A.U.= Arbitrary Units) along the X (or Y) and Z axes.

(D) Graph showing the percentage of circ-Hdgfrp3 dots included in TIAR and/or FUS granules in SK-N-BE cells. ***p < 0.01 corresponds to an unpaired two-tailed Student's t test. Error bars represent ±SEM (N = 3). All scale bars correspond to 10 μm.

specific overlapping probe. In such conditions, amplification can occur only on the circRNA, thus avoiding any amplification of the linear counterpart.

Although circRNAs have been extensively studied in the brain (D'Ambra et al., 2019), there are still only a few studies focusing on their specific subcellular localization in neuronal cells (Piwecka et al., 2017), and whether this changes in response to specific stimuli or pathological conditions (You et al., 2015).

In this work, we show that the MN-specific circ-Hdgfrp3 is present in neuronal processes, and that this localization increases with MN maturation when cells establish a dense neurite network.

Oxidative stress strongly affected such localization and caused circ-Hdgfrp3 retention at the perinuclear region. In control MNs, circ-Hdgfrp3 was found in assemblies related to SGs, while in MNs carrying the FUS-P517L mutation it was also associated to FUS-aggregates not related to SGs.

Even though mutant FUS-positive granules generally colocalize with SG markers (Bosco et al., 2010; Lenzi et al., 2015), our results are in line with other previous studies showing FUS-aggregates lacking or weakly associated with SG markers such as TIAR or G3BP (Kino et al., 2011; Shelkovnikova et al., 2014).

Moreover, 3D rendering and post-acquisition analyses showed an intimate connection of circ-Hdgfrp3 and mutant FUS that was not observed with TIAR. FUS-aggregates containing circ-Hdgfrp3 also associate with the p62/SQSTM1 protein, suggesting that these granules might eventually undergo degradation through autophagy. Interestingly, p62/SQSTM1 has been found associated to FUS inclusions in the brain and spinal cord of patients suffering from ALS and FTLD (Neumann et al., 2009; Lagier-Tourenne et al., 2010).

On the contrary, in our experimental conditions, ubiquitin was not detected in FUS-aggregates containing circ-Hdgfrp3 even though pathological FUS inclusions have been described to be immunoreactive for ubiquitin (Lagier-Tourenne et al., 2010). This can be explained by the timing and strength of the arsenite treatment applied in this study that cannot faithfully reproduce the conditions occurring in ALS patients.

TDP-43 was also not detected in FUS-aggregates. Although TDP-43 was detected in mutant FUS-aggregates when both proteins were overexpressed (Farrawell et al., 2015), it is generally absent in pathological FUS inclusions, in line with what we have observed.

Upon stress removal, circ-Hdgfrp3 only partially recovered its neurite localization from FUS mutant aggregates, suggesting that in ALS-associated conditions the long-lasting persistence of FUS-aggregates may have an impact on circRNA localization and function. Owing to the peculiar localization of circ-Hdgfrp3 in neurites, it is possible to envisage a function in the control of intracellular trafficking. While organelles such as mitochondria and endosomes utilize the microtubule-based motors kinesin and dynein for long-range transport, how membrane-less RNP granules are transported still remains a largely unexplored field. Recent work demonstrated that RNP particles can shuttle along neurites by hitchhiking to different types of organelles, such as lysosomes (Liao et al., 2019) or endosomes conjugated to mitochondria (Cioni et al., 2019); moreover, oxidative stress was shown to compromise anterograde transport of mitochondria and Golgi-related vesicles (Fang et al., 2012; Liao et al., 2017). These aspects are quite relevant in neuronal homeostasis because mutations in RNA binding proteins, molecular motors, and microtubule components have all been previously associated with neurodegeneration, underlining the important role of RNA transport to ensure long-standing neuronal function and integrity (Baird and Bennett, 2013).

Pathological aggregation in ALS and in other neurodegenerative diseases is a very well-studied phenomenon, which is driven by the propensity of several proteins involved in RNA metabolism and containing low complexity domains to form aggregates. However, recent studies indicate that the increase in concentration or the occurrence of specific mutations in these proteins are not the sole triggers of aggregate formation, but that RNA can also contribute toward the control of the phase transition of RNA-protein assemblies both in physiological (Van Treeck and Parker, 2018) and pathological conditions (Yin et al., 2009; Maharana et al., 2018; Kovachev et al., 2019).

Previous RNA sequencing analyses of SGs formed upon oxidative stress have shown that many different families of ncRNAs are recruited into this type of granule (Khong et al., 2017; Namkoong et al., 2018); however, the presence of circRNAs has not been described so far, even if some recent studies have shown circRNAs interacting with proteins involved in SG formation (Fischer et al., 2020). Here, we are able to show for the first time that circRNAs can also be present in such granules and that their localization can vary in response to a specific stress. Moreover, we found that this association is not a general feature of all circRNAs and is conserved between murine and human cells carrying a FUS mutation linked to a severe form of ALS.

Future work focused on the identification of circ-Hdgfrp3 interactors, could establish whether the circRNA moves as an autonomous RNP or whether specific organelles can mediate its transport; moreover, it could reveal how its trafficking contributes to MN activity and whether its alteration in stress conditions contributes to neurodegeneration.

Limitations of the study

In this study, we describe a powerful FISH approach, the Basescope, for the study of circRNA subcellular localization. This technology holds high specificity and allows the detection of transcripts expressed at

low levels even at single molecule. However, we could highlight a limitation of this approach: for a specific circRNA molecule we observed spots of different sizes. This could be due to either the presence of a variable number of circRNA molecules within each different spot or indeed to a limit of the technology. Because the Basescope is based on exponential probe amplification, this can result in the heterogeneous distribution of the probes giving rise to spots of different sizes. Finally, determining the physiological role of circ-Hdgfrp3 could have added more information about the possible correlation with the ALS pathology, indeed, this is currently under investigation and will be the focus of further studies.

STAR★METHODS

Detailed methods are provided in the online version of this paper and include the following:

- KEY RESOURCES TABLE
- RESOURCE AVAILABILITY
  - Lead contact
  - Materials availability
  - Data and code availability
- EXPERIMENTAL MODEL AND SUBJECT DETAILS
  - Cell cultures and differentiation
- METHOD DETAILS
  - Plasmid construction
  - Cell transfection
  - Sodium arsenite cell treatment
  - RNA fluorescence *in situ* hybridization and immunofluorescence
  - Confocal microscopy
  - Imaging analyses
  - RNA extraction and analyses
- QUANTIFICATION AND STATISTICAL ANALYSIS

SUPPLEMENTAL INFORMATION

Supplemental information can be found online at https://doi.org/10.1016/j.isci.2021.103504.

AUTHOR CONTRIBUTIONS

Conceptualization and design of the work were carried out by I.B. and M.M. The setting up of Basescope methodology was performed by E.D.A. and T.S. Microscopic analyses were performed by T.S., E.D.A., and E.V. The biological experiments were performed by E.D.A., E.V., V.S., and S.D.U. The original draft of the manuscript was written by E.D.A., M.M., and I.B. The draft was reviewed and edited by all the authors. All authors read and approved the final manuscript.

DECLARARTION OF INTEREST

The authors declare no competing interests.

REFERENCES

Abouzied, M.M., El-Tahir, H.M., Gieselmann, V., and Franken, S. (2010). Hepatoma-derived growth factor-related protein-3: a new neurotrophic and neurite outgrowth-promoting factor for cortical neurons. J. Neurosci. Res. *88*, 3610–3620. https://doi.org/10.1002/jnr.22507.

Ashwal-Fluss, R., Meyer, M., Pamudurti, N.R., Ivanov, A., Bartok, O., Hanan, M., Evantal, N., Memczak, S., Rajewsky, N., and Kadener, S. (2014). CircRNA biogenesis competes with pre-mRNA splicing. Mol.Cell *56*, 55–66. https://doi.org/10.1016/j.molcel.2014.08.019.

Baird, F.J., and Bennett, C.L. (2013). Microtubule defects & neurodegeneration. J. Genet. Syndr. Gene Ther. *4*, 203. https://doi.org/10.4172/2157-7412.1000203.

Baldwin, K.R., Godena, V.K., Hewitt, V.L., and Whitworth, A.J. (2016). Axonal transport defects are a common phenotype in Drosophila models of ALS. Hum. Mol. Genet. *25*, 2378–2392. https://doi.org/10.1093/hmg/ddw105.

Ballarino, M., Cipriano, A., Tita, R., Santini, T., Desideri, F., Morlando, M., Colantoni, A., Carrieri, C., Nicoletti, C., Musarò, A., et al. (2018). Deficiency in the nuclear long noncoding RNA Charme causes myogenic defects and heart remodeling in mice. EMBO J. *37*, e99697. https://doi.org/10.15252/embj.201899697.

Blair, I.P., Williams, K.L., Warraich, S.T., Durnall, J.C., Thoeng, A.D., Manavis, J., Blumbergs, P.C., Vucic, S., Kiernan, M.C., and Nicholson, G.A. (2010). FUS mutations in amyotrophic lateral sclerosis: clinical, pathological, neurophysiological and genetic analysis. J. Neurol. Neurosurg. Psychiatry *81*, 639–645. https://doi.org/10.1136/jnnp.2009.194399.

Bolte, S., and Cordelières, F.P. (2006). A guided tour into subcellular colocalization analysis in light microscopy. J. Microsc. *224*, 213–232. https://doi.org/10.1111/j.1365-2818.2006.01706.x.

Bosco, D.A., Lemay, N., Ko, H.K., Zhou, H., Burke, C., Kwiatkowski, T.J., Jr., Sapp, P., McKenna-Yasek, D., Brown, R.H., Jr., and Hayward, L.J. (2010). Mutant FUS proteins that cause amyotrophic lateral sclerosis incorporate into stress granules. Hum. Mol. Genet. *19*, 4160–4175. https://doi.org/10.1093/hmg/ddq335.

Capauto, D., Colantoni, A., Lu, L., Santini, T., Peruzzi, G., Biscarini, S., Morlando, M., Shneider, N.A., Caffarelli, E., Laneve, P., et al. (2018). A regulatory Circuitry between Gria2, miR-409, and miR-495 is affected by ALS FUS mutation in ESC-derived motor neurons. Mol. Neurobiol. *55*, 7635–7651. https://doi.org/10.1007/s12035-018-0884-4.

Chen, B.J., Huang, S., and Janitz, M. (2019). Changes in circular RNA expression patterns during human fetal brain development. Genomics *111*, 753–758. https://doi.org/10.1016/j.ygeno.2018.04.015.

Chiò, A., Restagno, G., Brunetti, M., Ossola, I., Calvo, A., Mora, G., Sabatelli, M., Monsurrò, M.R., Battistini, S., Mandrioli, J., et al. (2009). Two Italian kindreds with familial amyotrophic lateral sclerosis due to FUS mutation. Neurobiol. Aging *30*, 1272–1275. https://doi.org/10.1016/j.neurobiolaging.2009.05.001.

Cioni, J.M., Lin, J.Q., Holtermann, A.V., Koppers, M., Jakobs, M., Azizi, A., Turner-Bridger, B., Shigeoka, T., Franze, K., Harris, W.A., et al. (2019). Late endosomes act as mRNA translation platforms and sustain mitochondria in axons. Cell *176*, 56–72. https://doi.org/10.1016/j.cell.2018.11.030.

Conte, A., Lattante, S., Zollino, M., Marangi, G., Luigetti, M., Del Grande, A., Servidei, S., Trombetta, F., and Sabatelli, M. (2012). P525L FUS mutation is consistently associated with a severe form of juvenile amyotrophic lateral sclerosis. Neuromuscul. Disord. *22*, 73–75. https://doi.org/10.1016/j.nmd.2011.08.003.

D'Ambra, E., Capauto, D., and Morlando, M. (2019). Exploring the regulatory role of circular RNAs in neurodegenerative disorders. Int. J. Mol. Sci. *20*, 5477. https://doi.org/10.3390/ijms20215477.

De Vos, K.J., and Hafezparast, M. (2017). Neurobiology of axonal transport defects in motor neuron diseases: opportunities for translational research? Neurobiol. Dis. *105*, 283–299. https://doi.org/10.1016/j.nbd.2017.02.004.

Dormann, D., and Haass, C. (2011). TDP-43 and FUS: a nuclear affair. Trends Neurosci. *34*, 339–348. https://doi.org/10.1016/j.tins.2011.05.002.

Dormann, D., Rodde, R., Edbauer, D., Bentmann, E., Fischer, I., Hruscha, A., Than, M.E., Mackenzie, I.R., Capell, A., Schmid, B., et al. (2010). ALS-associated fused in sarcoma (FUS) mutations disrupt transportin-mediated nuclear import. EMBO J. *29*, 2841–2857. https://doi.org/10.1038/emboj.2010.143.

El-Tahir, H.M., Abouzied, M.M., Gallitzendoerfer, R., Gieselmann, V., and Franken, S. (2009). Hepatoma-derived growth factor-related protein-3 interacts with microtubules and promotes neurite outgrowth in mouse cortical neurons. J. Biol. Chem. *284*, 11637–11651. https://doi.org/10.1074/jbc.M901101200.

Erben, L., He, M.X., Laeremans, A., Park, E., and Buonanno, A. (2018). A novel ultrasensitive in situ hybridization approach to detect short sequences and splice variants with cellular resolution. Mol. Neurobiol. *55*, 6169–6181. https://doi.org/10.1007/s12035-017-0834-6.

Errichelli, L., Dini Modigliani, S., Laneve, P., Colantoni, A., Legnini, I., Capauto, D., Rosa, A., De Santis, R., Scarfò, R., Peruzzi, G., et al. (2017). FUS affects circular RNA expression in murine embryonic stem cell-derived motor neurons. Nat. Commun. *8*, 1–11. https://doi.org/10.1038/ncomms14741.

Fanale, D., Taverna, S., Russo, A., and Bazan, V. (2018). Circular RNA in exosomes. Adv. Exp. Med. Biol. *1087*, 109–117. https://doi.org/10.1007/978-981-13-1426-1_9.

Fang, C., Bourdette, D., and Banker, G. (2012). Oxidative stress inhibits axonal transport: implications for neurodegenerative diseases.

Mol. Neurodegener. *7*, 29. https://doi.org/10.1186/1750-1326-7-29.

Farrawell, N.E., Lambert-Smith, I.A., Warraich, S.T., Blair, I.P., Saunders, D.N., Hatters, D.M., and Yerbury, J.J. (2015). Distinct partitioning of ALS associated TDP-43, FUS and SOD1 mutants into cellular inclusions. Sci. Rep. *5*, 13416. https://doi.org/10.1038/srep13416.

Fischer, J.W., Busa, V.F., Shao, Y., and Leung, A.K.L. (2020). Structure-Mediated RNA decay by UPF1 and G3BP1. Mol.Cell *78*, 70–84. https://doi.org/10.1016/j.molcel.2020.01.021.

Gardiner, J., Overall, R., and Marc, J. (2013). The nervous system cytoskeleton under oxidative stress. Diseases *1*, 36–50. https://doi.org/10.3390/diseases1010036.

Guo, W., Naujock, M., Fumagalli, L., Vandoorne, T., Baatsen, P., Boon, R., Ordovás, L., Patel, A., Welters, M., Vanwelden, T., et al. (2017). HDAC6 inhibition reverses axonal transport defects in motor neurons derived from FUS-ALS patients. Nat. Commun. *8*, 861. https://doi.org/10.1038/s41467-017-00911-y.

Guo, X., Zhao, Y., Nguyen, H., Liu, T., Wang, Z., and Lou, H. (2018). Quantitative analysis of alternative pre-mRNA splicing in mouse brain sections using RNA in situ hybridization assay. J. Vis. Exp. *57889*. https://doi.org/10.3791/57889.

Hansen, T.B., Jensen, T.I., Clausen, B.H., Bramsen, J.B., Finsen, B., Damgaard, C.K., and Kjems, J. (2013). Natural RNA circles function as efficient microRNA sponges. Nature *495*, 384–388. https://doi.org/10.1038/nature11993.

Hosaka, T., Yamashita, T., Tamaoka, A., and Kwak, S. (2019). Extracellular RNAs as biomarkers of sporadic amyotrophic lateral sclerosis and other neurodegenerative diseases. Int. J. Mol. Sci. *20*, 3148. https://doi.org/10.3390/ijms20133148.

Jeck, W.R., Sorrentino, J.A., Wang, K., Slevin, M.K., Burd, C.E., Liu, J., Marzluff, W.F., and Sharpless, N.E. (2013). Circular RNAs are abundant, conserved, and associated with ALU repeats. RNA *19*, 141–157. https://doi.org/10.1261/rna.035667.112.

Kedersha, N.L., Gupta, M., Li, W., Miller, I., and Anderson, P. (1999). RNA-binding proteins TIA-1 and TIAR link the phosphorylation of eIF-2 alpha to the assembly of mammalian stress granules. J.Cell Biol. *147*, 1431–1442. https://doi.org/10.1083/jcb.147.7.1431.

Khong, A., Matheny, T., Jain, S., Mitchell, S.F., Wheeler, J.R., and Parker, R. (2017). The stress granule transcriptome reveals principles of mRNA accumulation in stress granules. Mol.Cell *68*, 808–820. https://doi.org/10.1016/j.molcel.2017.10.015.

Kino, Y., Washizu, C., Aquilanti, E., Okuno, M., Kurosawa, M., Yamada, M., Doi, H., and Nukina, N. (2011). Intracellular localization and splicing regulation of FUS/TLS are variably affected by amyotrophic lateral sclerosis-linked mutations. Nucleic Acids Res. *39*, 2781–2798. https://doi.org/10.1093/nar/gkq1162.

Kocks, C., Boltengagen, A., Piwecka, M., Rybak-Wolf, A., and Rajewsky, N. (2018). Single-molecule fluorescence in situ hybridization (FISH) of circular RNA CDR1as. Methods Mol. Biol. *1724*, 77–96. https://doi.org/10.1007/978-1-4939-7562-4_7.

Kovachev, P.S., Gomes, M.P.B., Cordeiro, Y., Ferreira, N.C., Valadão, L.P.F., Ascari, L.M., Rangel, L.P., Silva, J.L., and Sanyal, S. (2019). RNA modulates aggregation of the recombinant mammalian prion protein by direct interaction. Sci. Rep. *9*, 12406. https://doi.org/10.1038/s41598-019-48883-x.

Kwiatkowski, T.J., Bosco, D.A., LeClerc, A.L., Tamrazian, E., Vanderburg, C.R., Russ, C., Davis, A., Gilchrist, J., Kasarskis, E.J., Munsat, T., et al. (2009). Mutations in the FUS/TLS gene on chromosome 16 cause familial amyotrophic lateral sclerosis. Science *323*, 1205–1208. https://doi.org/10.1126/science.1166066.

Lagier-Tourenne, C., Polymenidou, M., and Cleveland, D.W. (2010). TDP-43 and FUS/TLS: emerging roles in RNA processing and neurodegeneration. Hum. Mol. Genet. *19*, R46–R64. https://doi.org/10.1093/hmg/ddq137.

Lasda, E., and Parker, R. (2016). Circular RNAs Co-precipitate with extracellular vesicles: a possible mechanism for circRNA Clearance. PLoS One *11*, e0148407. https://doi.org/10.1371/journal.pone.0148407.

Legnini, I., Di Timoteo, G., Rossi, F., Morlando, M., Briganti, F., Sthandier, O., Fatica, A., Santini, T., Andronache, A., Wade, M., et al. (2017). Circ-ZNF609 is a circular RNA that can Be translated and functions in myogenesis. Mol.Cell *66*, 22–37. https://doi.org/10.1016/j.molcel.2017.02.017.

Lenzi, J., De Santis, R., De Turris, V., Morlando, M., Laneve, P., Calvo, A., Caliendo, V., Chiò, A., Rosa, A., and Bozzoni, I. (2015). ALS mutant FUS proteins are recruited into stress granules in induced pluripotent stem cell-derived motoneurons. Dis.Model Mech. *8*, 755–766. https://doi.org/10.1242/dmm.020099.

Li, Z., Huang, C., Bao, C., Chen, L., Lin, M., Wang, X., Zhong, G., Yu, B., Hu, W., Dai, L., et al. (2015). Exon-intron circular RNAs regulate transcription in the nucleus. Nat. Struct. Mol. Biol. *22*, 256–264. https://doi.org/10.1038/nsmb.2959.

Liao, Y.-C., Fernandopulle, M.S., Wang, G., Choi, H., Hao, L., Drerup, C.M., Patel, R., Qamar, S., Nixon-Abell, J., Shen, Y., et al. (2019). RNA granules hitchhike on lysosomes for long-distance transport, using annexin A11 as a molecular tether. Cell *79*, 147–164. https://doi.org/10.1016/j.cell.2019.08.050.

Liao, P.C., Tandarich, L.C., and Hollenbeck, P.J. (2017). ROS regulation of axonal mitochondrial transport is mediated by Ca2+ and JNK in Drosophila. PLoS One *12*, e017810. https://doi.org/10.1371/journal.pone.0178105.

Liu, C.X., Li, X., Nan, F., Jiang, S., Gao, X., Guo, S.K., Xue, W., Cui, Y., Dong, K., Ding, H., et al. (2019). Structure and degradation of circular RNAs regulate PKR activation in innate immunity. Cell *177*, 865–880. https://doi.org/10.1016/j.cell.2019.03.046.

Lukiw, W.J. (2013). Circular RNA (circRNA) in Alzheimer's disease (AD). Front Genet. *4*, 307. https://doi.org/10.3389/fgene.2013.00307.

Maharana, S., Wang, J., Papadopoulos, D.K., Richter, D., Pozniakovsky, A., Poser, I., Bickle, M., Rizk, S., Guillén-Boixet, J., Franzmann, T.M., et al. (2018). RNA buffers the phase separation behavior of prion-like RNA binding proteins. Science *360*, 918–921. https://doi.org/10.1126/science.aar7366.

Mahmoudi, E., and Cairns, M.J. (2019). Circular RNAs are temporospatially regulated throughout development and ageing in the rat. Sci. Rep. *9*, 2564. https://doi.org/10.1038/s41598-019-38860-9.

Memczak, S., Jens, M., Elefsinioti, A., Torti, F., Krueger, J., Rybak, A., Maier, L., Mackowiak, S.D., Gregersen, L.H., Munschauer, M., et al. (2013). Circular RNAs are a large class of animal RNAs with regulatory potency. Nature *495*, 333–338. https://doi.org/10.1038/nature11928.

Morlando, M., Dini Modigliani, S., Torrelli, G., Rosa, A., Di Carlo, V., Caffarelli, E., and Bozzoni, I. (2012). FUS stimulates microRNA biogenesis by facilitating co-transcriptional Drosha recruitment. EMBO J. *31*, 4502–4510. https://doi.org/10.1038/emboj.2012.319.

Mortazavi, A., Williams, B.A., McCue, K., Schaeffer, L., and Wold, B. (2008). Mapping and quantifying mammalian transcriptomes by RNA-Seq. Nat. Methods *5*, 621–628. https://doi.org/10.1038/nmeth.1226.

Namkoong, S., Ho, A., Woo, Y.M., Kwak, H., and Lee, J.H. (2018). Systematic characterization of stress-induced RNA granulation. Mol.Cell *70*, 175–187. https://doi.org/10.1016/j.molcel.2018.02.025.

Neumann, M., Rademakers, R., Roeber, S., Baker, M., Kretzschmar, H.A., and Mackenzie, I.R. (2009). A new subtype of frontotemporal lobar degeneration with FUS pathology. Brain *132*, 2922–2931. https://doi.org/10.1093/brain/awp214.

Orjalo, A.V., Jr., and Johansson, H.E. (2016). Stellaris® RNA fluorescence in situ hybridization for the simultaneous detection of immature and mature long noncoding RNAs in adherent cells. Methods Mol. Biol. *1402*, 119–134. https://doi.org/10.1007/978-1-4939-3378-5_10.

Pamudurti, N.R., Bartok, O., Jens, M., Ashwal-Fluss, R., Stottmeister, C., Ruhe, L., Hanan, M., Wyler, E., Perez-Hernandez, D., Ramberger, E., et al. (2017). Translation of CircRNAs. Mol.Cell *66*, 9–21. https://doi.org/10.1016/j.molcel.2017.02.021.

Piwecka, M., Glažar, P., Hernandez-Miranda, L.R., Memczak, S., Wolf, S.A., Rybak-Wolf, A., Filipchyk, A., Klironomos, F., Cerda Jara, C.A., Fenske, P., et al. (2017). Loss of a mammalian circular RNA locus causes miRNA deregulation and affects brain function. Science *357*, eaam8526. https://doi.org/10.1126/science.aam8526.

Rossi, F., Legnini, I., Megiorni, F., Colantoni, A., Santini, T., Morlando, M., Di Timoteo, G., Dattilo, D., Dominici, C., and Bozzoni, I. (2019). Circ-ZNF609 regulates G1-S progression in

rhabdomyosarcoma. Oncogene *38*, 3843–3854. https://doi.org/10.1038/s41388-019-0699-4.

Rybak-Wolf, A., Stottmeister, C., Glažar, P., Jens, M., Pino, N., Giusti, S., Hanan, M., Behm, M., Bartok, O., Ashwal-Fluss, R., et al. (2014). Circular RNAs in the mammalian brain are highly abundant, conserved, and dynamically expressed. Mol.Cell *58*, 870–885. https://doi.org/10.1016/j.molcel.2015.03.027.

Salvatori, B., Biscarini, S., and Morlando, M. (2020). Non-coding RNAs in nervous system development and disease. Front Cell Dev. Biol. *8*, 273. https://doi.org/10.3389/fcell.2020.00273.

Salzman, J., Gawad, C., Wang, P.L., Lacayo, N., and Brown, P.O. (2012). Circular RNAs are the predominant transcript isoform from hundreds of human genes in diverse cell types. PLoS One *7*, e30733. https://doi.org/10.1371/journal.pone.0030733.

Sama, R.R.K., Fallini, C., Gatto, R., McKeon, J.E., Song, Y., Rotunno, M.S., Penaranda, S., Abdurakhmanov, I., Landers, J.E., Morfini, G., et al. (2017). ALS-linked FUS exerts a gain of toxic function involving aberrant p38 MAPK activation. Sci. Rep. *7*, 115. https://doi.org/10.1038/s41598-017-00091-1.

Schneider, C.A., Rasband, W.S., and Eliceiri, K.W. (2012). NIH Image to ImageJ: 25 years of image analysis. Nat. Methods *9*, 671–675. https://doi.org/10.1038/nmeth.2089.

Shelkovnikova, T.A., Robinson, H.K., Southcombe, J.A., Ninkina, N., and Buchman, V.L. (2014). Multistep process of FUS aggregation in the cell cytoplasm involves RNA-dependent and RNA-independent mechanisms. Hum. Mol. Genet. *23*, 5211–5226. https://doi.org/10.1093/hmg/ddu243.

Taylor, J.P., Brown, R.H., Jr., and Cleveland, D.W. (2016). Decoding ALS: from genes to mechanism. Nature *539*, 197–206. https://doi.org/10.1038/nature20413.

Van Treeck, B., and Parker, R. (2018). Emerging roles for intermolecular RNA-RNA interactions in RNP assemblies. Cell *174*, 791–802. https://doi.org/10.1016/j.cell.2018.07.023.

Vance, C., Rogelj, B., Hortobágyi, T., De Vos, K.J., Nishimura, A.L., Sreedharan, J., Hu, X., Smith, B., Ruddy, D., Wright, P., et al. (2009). Mutations in FUS, an RNA processing protein, cause familial amyotrophic lateral sclerosis type 6. Science *323*, 1208–1211. https://doi.org/10.1126/science.1165942.

Veno, M.T., Hansen, T.B., Venø, S.T., Clausen, B.H., Grebing, M., Finsen, B., Holm, I.E., and Kjems, J. (2015). Spatio-temporal regulation of circular RNA expression during porcine embryonic brain development. Genome Biol. *6*, 1–17. https://doi.org/10.1186/s13059-015-0801-3.

Wang, P.L., Bao, Y., Yee, M.C., Barrett, S.P., Hogan, G.J., Olsen, M.N., Dinneny, J.R., Brown, P.O., and Salzman, J. (2014). Circular RNA is expressed across the eukaryotic tree of life. PLoS One *9*, e90859. https://doi.org/10.1371/journal.pone.0090859.

Wang, Z., Xu, P., Chen, B., Zhang, Z., Zhang, C., Zhan, Q., Huang, S., Xia, Z.A., and Peng, W.

(2018). Identifying circRNA-associated-ceRNA networks in the hippocampus of Aβ1-42-induced Alzheimer's disease-like rats using microarray analysis. Aging 10, 775–788. https://doi.org/10.18632/aging.101427.

Westholm, J.O., Miura, P., Olson, S., Shenker, S., Joseph, B., Sanfilippo, P., Celniker, S.E., Graveley, B.R., and Lai, E.C. (2014). Genome-wide analysis of Drosophila circular RNAs reveals their structural and sequence properties and age-dependent neural accumulation. Cell Rep. 9, 1966–1980. https://doi.org/10.1016/j.celrep.2014.10.062.

Wichterle, H., and Peljto, M. (2008). Differentiation of mouse embryonic stem cells to spinal motor neurons. Curr. Protoc. Stem Cell

Biol. 5, 1–9. https://doi.org/10.1002/9780470151808.sc01h01s5.

Williamson, T.L., and Cleveland, D.W. (1999). Slowing of axonal transport is a very early event in the toxicity of ALS-linked SOD1 mutants to motor neurons. Nat. Neurosci. 2, 50–56. https://doi.org/10.1038/4553.

Wilusz, J.E. (2018). A 360° view of circular RNAs: from biogenesis to functions. Wiley Interdiscip. Rev. RNA 9, e1478. https://doi.org/10.1002/wrna.1478.

Wu, C.Y., Whye, D., Mason, R.W., and Wang, W. (2012). Efficient differentiation of mouse embryonic stem cells into motor neurons. J. Vis. Exp. 64, e3813. https://doi.org/10.3791/3813.

Yin, J., Chen, R., and Liu, C. (2009). Nucleic acid induced protein aggregation and its role in biology and pathology. Front Biosci. 14, 5084–5106. https://doi.org/10.2741/3588.

You, X., Vlatkovic, I., Babic, A., Will, T., Epstein, I., Tushev, G., Akbalik, G., Wang, M., Glock, C., Quedenau, C., et al. (2015). Neural circular RNAs are derived from synaptic genes and regulated by development and plasticity. Nat. Neurosci. 18, 603–610. https://doi.org/10.1038/nn.3975.

Zhou, L., Li, Y., and Yue, B.Y. (1999). Oxidative stress affects cytoskeletal structure and cell-matrix interactions in cells from an ocular tissue: the trabecular meshwork. J. Cell Physiol. 180, 182–1889. https://doi.org/10.1002/(SICI)1097-4652(199908)180:2<182::AID-JCP6>3.0.CO;2-X.

STAR★METHODS

KEY RESOURCES TABLE

REAGENT or RESOURCE	SOURCE	IDENTIFIER
Antibodies		
Rabbit polyclonal anti-TLS/FUS	Abcam	cat#ab84078; RRID:AB_2105201
Mouse monoclonal anti-TIAR	BD Transduction Laboratories	cat#610352; RRID:AB_397742
Mouse monoclonal anti-ISLET 1/2	DSHB	cat#39.4D5; RRID:AB_2314683
Mouse monoclonal anti-β TUBIII	Sigma-Aldrich	cat#T2200; RRID:AB_262133
Rabbit polyclonal anti-TDP43	Proteintech	cat#10782-2-AP
Rabbit polyclonal anti-p62/SQSTM1	Santa Cruz Biotechnology	cat#D-3 sc-28359
Rabbit polyclonal anti-ubiquitin DAKO	Labome	cat#Z0458
Goat anti-Mouse IgG (H+L) Cross-Adsorbed Secondary Antibody, Alexa Fluor 488	ThermoFisher Scientific	cat#A11001; RRID:AB_2534069
Goat anti-Rabbit IgG (H+L) Cross-Adsorbed Secondary Antibody, Alexa Fluor 488	ThermoFisher Scientific	cat#A11008; RRID:AB_143165
Donkey anti-Mouse IgG (H+L) Highly Cross-Adsorbed Secondary Antibody, Alexa Fluor Plus 647	ThermoFisher Scientific	cat#A32787; RRID:AB_2762830
Donkey anti-Rabbit IgG (H+L) Highly Cross-Adsorbed Secondary Antibody, Alexa Fluor Plus 647	ThermoFisher Scientific	cat#A32795; RRID:AB_2762835
Bacterial and virus strains		
HIT-DH5alpha JUMBO 107	BioAspect	cat#BA-RH617-J
Chemicals, peptides, and recombinant proteins		
Sodium Arsenite	Sigma-Aldrich	cat#S7400
Doxycycline hyclate	Sigma-Aldrich	cat#D9891
Paraformaldehyde	Electron Microscopy Sciences, Hatfield, PA	cat#15710
Papain	Worthington Biochemical Corporation	cat#LK003176
Ovomucoid inhibitor-Albumin	Worthington Biochemical Corporation	cat#LK003182
Sterile Earle's Balanced Salt Solution (EBSS)	Sigma-Aldrich	cat#E7510
Poly-L-ornithine	Sigma-Aldrich	cat#P-3655
Murine Laminin	Sigma-Aldrich	cat#L2020
Collagen Type I rat tail	Ibidi	cat#50201
2-mercaptoethanol for ES cells	Sigma-Aldrich	cat#ES-007-E
Embryonic stem-cell FBS, qualified, US origin	ThermoFisher Scientific	cat#16141079
EmbryoMax DMEM	Sigma-Aldrich	cat#SLM-220-B
EmbryoMax 100X nucleosides for ES cells	Sigma-Aldrich	cat#ES-008-D
EmbryoMax non-essential a.a.	Sigma-Aldrich	cat#TMS-001-C
ESGRO® Recombinant Mouse LIF Protein	Chemicon	cat#ESG11107
PD173074	Sigma-Aldrich	cat# P2499
GSK-3 Inhibitor XVI	Sigma-Aldrich	cat#361559
Advanced DMEM/F12	Gibco	cat#12634010
Neurobasal™ Medium	Gibco	cat#21103049
Dulbecco's Modified Eagle's Medium/Nutrient Mixture F-12 Ham	ThermoFisher Scientific	cat#D6421

Continued

REAGENT or RESOURCE	SOURCE	IDENTIFIER
D-(+)-Glucose solution	Sigma-Aldrich	cat#G8769
Horse serum	ThermoFisher Scientific	cat#16050122
Deoxyribonuclease I from bovine pancreas	Sigma-Aldrich	cat#DN25
N-2 supplement	Gibco	cat#17502-001
GlutaMAX™Supplement	ThermoFisher Scientific	cat#35050061
B-27™Supplement (50X), serum free	ThermoFisher Scientific	cat#17504001
Smoothened agonist, SAG	Sigma-Aldrich	cat#566660
Retinoic Acid	Sigma-Aldrich	cat#R2625
KnockOut™ Serum Replacement	ThermoFisher Scientific	cat#10828028
L-ascorbic acid	Sigma-Aldrich	cat#TMS-001-C
Trypan blue solution	ThermoFisher Scientific	cat#15250061
L-glutamine	Sigma-Aldrich	cat#G7513
Recombinant Human GDNF	Peprotech	cat#450-44
Recombinant Human CNTF	Peprotech	cat#AF-450-13
Recombinant Human/Murine/Rat BDNF	Peprotech	cat#450-02
Y-27632 dihydrochloride	Sigma-Aldrich	cat#Y0503
Penicillin/Streptomycin	Sigma-Aldrich	cat#P0781
FBS	Sigma-Aldrich	cat#F7524
DMEM- High glucose	Sigma-Aldrich	cat#D6546
Opti-MEM™ Reduced Serum Medium	Thermo Fisher Scientific	cat#31985070
Lipofectamine™ 2000 Transfection Reagent	Thermo Fisher Scientific	cat#11668019
Lipofectamine™ RNAiMAX Transfection Reagent	Thermo Fisher Scientific	cat#13778075
RPMI-1640	Sigma-Aldrich	cat#R8758
Sodium Pyruvate	Thermo Fisher Scientific	cat#11360070
Fetal Bovine Serum, qualified, USA	Gibco	cat# LS26140079
all-trans-Retinoic Acid	Sigma-Aldrich	cat#554720
PBS	Sigma-Aldrich	N/A
Bovin Serum Albumin	Sigma-Aldrich	cat#A9418
Triton X-100	Sigma-Aldrich	cat#9002-93-1
CloneAmp™ HiFi PCR Premix	Clontech	cat#639298
PrimeScript RT Master Mix	TakaraBio	cat#RR036b
PowerUp SYBR-Green MasterMix	Thermo Fisher Scientific	cat#4385612
Goat serum	Sigma-Aldrich	cat#G9023
Donkey serum	Sigma-Aldrich	cat#D9663
Protease III	ACD	cat#322381
RNAscope Wash Buffer Reagents	ACD	cat#310091
DAPI solution	Sigma-Aldrich	cat#D9542
ProLong Diamond Antifade Mountant	Thermo Fisher Scientific	cat#P-36961
Critical commercial assays		
In-Fusion® HD Cloning Kit	TakaraBio	cat#102518
Direct-Zol RNA MiniPrep Kit	Zymo Research	cat#R2050
BaseScope™ Detection Reagent Kit v2	ACD	cat#323910
RNAscope pretreatment reagents	ACD	cat#322381

Continued

REAGENT or RESOURCE	SOURCE	IDENTIFIER
Experimental models: Cell lines		
Mouse: HBG3 ES cell line carrying an Hb9-GFP transgene	Provided by Prof. Niel A. Shneider (Columbia University).	N/A
Mouse: mESCs carrying FUS P517L mutation in homozygosity	Provided by Prof. Niel A. Shneider (Columbia University)	N/A
Mouse: Neuro-2a (N2a)	ATCC	cat#CCL-131™
Human: SK-N-BE cell lines expressing of the transgenes WT FUS and FUS-P525L	(Morlando et al., 2012)	N/A
Oligonucleotides		
DNA oligonucleotides for qPCR experiments used in this work, see Table S1	This paper	N/A
siRNAs for cell transfection used in this work: Dharmacon ON-TARGETplus targeting the circ-Hdgfrp3 BSJ (Sense sequence: 5'-CGG UGAAGGGAUUGAUGAAUU-3', Antisense sequence: 5'-UUCAUCAAUCCCUUCAC CGUU-3'); scramble RNA (Non-targeting Pool #D-001810-10-20)	This paper	N/A
DNA oligonucleotides used to clone human circ-Hdgfrp3 into p-circ-3xF expression vector, see Table S2	This paper	N/A
Custom DNA circ-Hdgfrp3-specific probe for BaseScope™	This paper	cat#703021
Negative control probe DapB for BaseScope™	(Rossi et al., 2019)	cat#701021
Custom DNA circ-ZNF609-specific probe for BaseScope™	(Rossi et al., 2019)	cat#708461
Recombinant DNA		
p-circ-3xF used for cloning human circ-Hdgfrp3 expression vector	(Legnini et al., 2017)	N/A
p-circ-Hdgfrp3 vector used for the expression of human circ-Hdgfrp3	This paper	N/A
Software and algorithms		
SDS Applied Biosystem 7500 Fast Real-Time PCR system software	ThermoFisher Scientific	N/A
ImageJ software	(Schneider et al., 2012)	https://imagej.nih.gov/ij/download.html
MetaMorph® Microscopy Automation and Image Analysis Software	Molecular Devices	RRID:SCR_002368; https://www.moleculardevices.com/products/cellular-imaging-systems/acquisition-and-analysis-software/metamorph-microscopy#gref
ImageJ Plot "Z-axis profiler" plugin	DimiterProdanov;ZAxis_Profiler.java	https://imagej.nih.gov/ij/plugins/dynamic-profiler/index.html
ImageJ "3D viewer" plugin	Benjamin Schmid;ImageJ_3D_Viewer.jar	https://imagej.nih.gov/ij/plugins/3d-viewer/
ImageJ "JACoP (Just Another Colocalization Plugin)" plugin	Fabrice P. Cordelieres, Institut Curie, Orsay (France)(Bolte and Cordelières., 2006)	https://imagej.nih.gov/ij/plugins/track/jacop.html

RESOURCE AVAILABILITY

Lead contact

Further information and requests for resources and reagents should be directed to and will be fulfilled by the lead contact, Irene Bozzoni (irene.bozzoni@uniroma1.it).

Materials availability

All unique/stable reagents generated in this study are available from the lead contact upon request.

Data and code availability

- All data reported in this paper will be shared by the lead contact upon request.

- This paper does not report original code.

- Any additional information required to reanalyze the data reported in this paper is available from the lead contact upon request.

EXPERIMENTAL MODEL AND SUBJECT DETAILS

Cell cultures and differentiation

All cell lines used in this study were grown at 37°C, 5% CO_2. All cell lines were tested for mycoplasma contamination.

Murine HBG3 ES cells (embryonic stem cells derived from HB9::GFP transgenic mice) were cultured and differentiated into spinal motor neurons (MNs) as described in Wichterle and Peljto, 2008 and Capauto et al., 2018. Briefly, cells were maintained in culture with mESC medium, composed by EmbryoMax DMEM, 15% Embryonic stem-cell FBS (ThermoFisher Scientific), 1% EmbryoMax 100X nucleosides (Sigma-Aldrich), 1% EmbryoMax non-essential amino acids (Sigma-Aldrich), 2-mercaptoethanol for ES cells (Sigma-Aldrich), 2 mM L-glutamine (Sigma-Aldrich) and 1% penicillin-streptomycin (Sigma-Aldrich), supplied with ESGRO Recombinant Mouse LIF Protein (Chemicon) and 2i (PD173074 from Sigma-Aldrich and GSK-3 Inhibitor XVI from Sigma-Aldrich). For motoneuronal differentiation, HBG3 ES cell-derived EBs (embryoid bodies) obtained after 6 days of MN differentiation in ADNFK medium (Capauto et al., 2018).

Generation of embryoid bodies (EBs) was obtained by culturing mESCs in ADNFK medium (1:1) Advanced DMEM/F12 (Gibco):Neurobasal medium (Gibco), 10% Knock Out Serum Replacement (Gibco), 1% Gluta-MAX, 1% 2-mercaptoethanol, 1% Pen/Strep). On day 2, ADNFK medium was supplemented with 2% B27 Supplement (Gibco), 1μM RA (Sigma Aldrich) and 0.5 μM SAG (Merck Millipore). On day 5, ADNFK medium was supplemented with 2% B27 Supplement and 5 ng/mL GDNF (Peprotech). On day 6, EBs were dissociated following the manufacturer's instructions: incubated with 20U/ml Papain (Worthington Biochemical Corporation), agitated for 5 minutes by hand and then blocked with 10 mg/ml ovomucoid inhibitor (Worthington Biochemical Corporation) for 5 min. After cells precipitated into a pellet by gravity, supernatant was removed and cells were resuspended and triturated in PBS supplemented with 0.4% Glucose (Sigma) 2.5% horse serum (Thermofisher scientific), 2% B27, 3mM $MgCl_2$, Deoxyribonuclease I (Sigma-Aldrich, 25μg/ml). Single cells were then plated on 0.01% poly-L-ornithine (Sigma-Aldrich), Murine Laminin 20 μg/mL (Sigma) and maintained in culture with N2B27 medium (50 % DMEM/F-12 Ham, 50 % Neurobasal Medium, 1% GlutaMAX Supplement, 1% 2-mercaptoethanol, 1% non-essential amino acids, 0.5 % penicillin-streptomycin) supplemented with 2% N-2 supplement (Gibco), 1% B-27 supplement serum free (ThermoFisher Scientific), 200 ng/mL L-ascorbic acid (Sigma-Aldrich), 20 ng/mL BDNF (Peprotech), 10 ng/mL GDNF (Peprotech) and 10 ng/mL CNTF (Peprotech) and 10 mM ROCK inhibitor (Y-27632 dihydrochloride; Sigma-Aldrich).

Murine Neuro-2a cells (ATCC, Cat. No. CCL-131) were cultured in DMEM high-glucose medium (Sigma-Aldrich) supplemented with 10% Fetal Bovine Serum (Sigma-Aldrich), L-glutamine (Sigma-Aldrich), 1% penicillin-streptomycin (Sigma-Aldrich). When subjected to cell fixation and imaging analyses, N2a cells were plated on pre-coated glass coverslips (22.5 μg/ml Collagen Type I rat tail, Ibidi).

Human SK-N-BE cells expressing WT FUS and FUS-P525L transgenes (Morlando et al., 2012) were cultured in RPMI 1640 medium (Sigma-Aldrich) supplemented with 10% FBS, 1% sodium pyruvate, 1% glutamax and 1% penicillin-streptomycin. SK-N-BE cells were differentiated for 6 days with medium containing 10 μM all-trans-retinoic acid (Sigma-Aldrich) and 2.5% heat inactivated Foetal Bovine Serum, qualified, USA (Gibco). The expression of the different forms of FUS protein was induced by adding doxycycline (0.2 μg/ml) to the culture medium 24 hours prior harvesting.

METHOD DETAILS

Plasmid construction

p-circ-Hdgfrp3 plasmid, used for the expression of human circ-Hdgfrp3, was obtained using p-circ-3xF (Legnini et al., 2017) as backbone. Circ-Hdgfrp3 DNA sequence (exons 2-3-4-5) was PCR-amplified from SK-N-BE cDNA using CloneAmp HiFi PCR Premix (Clontech) while the p-circ-3xF was linearized by inverted PCR using CloneAmp HiFi PCR Premix (Clontech). The oligonucleotides used for cloning are listed in Table S1. The final plasmid p-circ-Hdgfrp3 was obtained using the In-Fusion HD Cloning Plus kit (Takara Bio) following manufacturer's instructions.

Cell transfection

For N2a transfections, siRNAs (Dharmacon-ON-TARGETplus) targeting the circ-Hdgfrp3 backsplicing junction (siRNA sense sequence: 5'-CGGUGAAGGGAUUGAUGAAUU-3'; siRNA antisense sequence: 5'-UUCAUCAA UCCCUUCACCGUU-3') or a scramble RNA (Non-targeting Pool #D-001810-10-20) were employed. $3x10^5$ cells plated in 3.5-cm culture dishes were transfected either with 50 nM of si-Circ or si-SCR, previously incubated 20 minutes with 3 µl Lipofectamine RNAiMAX Reagent (ThermoFisher Scientific) and 150 µl Opti-MEM. The mixture was added to cells in 2 ml fresh medium and cells were harvested after 48 hours of transfection.

To achieve circ-Hdgfrp3 overexpression in differentiated SK-N-BE cells expressing WT or FUS P525L mutant protein, 3 µg of p-circ-Hdgfrp3 vector were added to 150 µl Opti-MEM reduced serum medium (ThermoFisher Scientific), and 3 µl Lipofectamine 2000 (ThermoFisher Scientific) were mixed with other 150 µl Opti-MEM, separately. The two mixtures were briefly vortexed and left 5 min at room temperature, then they were mixed again and after another 20 min at room temperature they were added to cells in 2 ml fresh medium. Medium was replaced the day after, and cells were harvested 48 h after transfection.

Sodium arsenite cell treatment

To apply oxidative stress on single cell-plated ES-derived MNs (MN-d2; day 2 after EB dissociation), 0.5 mM sodium arsenite (ARS; Sigma-Aldrich, S7400) was added to the cell media for 60 minutes at 37°C. For recovery experiments, media containing ARS was replaced with fresh media lacking ARS. Cells were fixed after 240 minutes of recovery.

In SK-N-BE cells, oxidative stress was applied by using 0.5 mM ARS for 90 minutes at 37°C. Untreated cells were used to control each condition in all experiments. Detailed information about the cell fixation used in this work are provided in the following section.

RNA fluorescence *in situ* hybridization and immunofluorescence

Cells cultured on pre-coated glass coverslips (0.01% poly-L-ornithine, Sigma-Aldrich, 20 µg/mL murine Laminin, Sigma-Aldrich) were fixed in 4% paraformaldehyde (Electron Microscopy Sciences, Hatfield, PA) in PBS for 20 min at 4°C. Following the dehydration steps with the ice-cold ethanol series (50%, 70%, 100%), cells were stored at −20°C in absolute ethanol until use. Detection of circ-Hdgfrp3 was performed via Basescope™ assay (Advanced Cell Diagnostics, Bio-Techne) as previously described in Rossi et al. (2019), with a little modification. Briefly, fixed cells were permeabilized with Protease III (diluted 1:15; ref. 322381) before hybridization with the circ-Hdgfrp3-specific probes, at 40°C for 2 hours. Probes used to detect circ-Hdgfrp3 (ref. 703021) were custom produced by Advanced Cell Diagnostics and designed to specifically target the backsplicing junction of the circular RNA. A probe specific for the bacterial RNA DapB was used as negative control (ref. 701021) while the circ-ZNF609-specific probe (ref. 708461) employed by Rossi et al. (2019) was used to detect a circRNA that is not regulated by FUS.

Amplification and detection steps were performed in accordance with the manufacturer's instructions by using Basescope™ detection reagents V2– RED (ref. 323910). After each amplification step, three washes were performed with 300 ml of 1X RNAscope Wash Buffer Reagents (ref. 310091) for 5 minutes at room temperature.

When FISH staining was combined with Immunofluorescence, cells were incubated with the following primary antibodies: anti-FUS (Abcam, ab84078) diluted 1:100; Anti-TIAR (BD Transduction Laboratories, 610352) diluted 1:200, anti-ISLET 1/2 (DSHB, 39.4D5) diluted 1:25, anti-β TUBIII (Sigma, T2200) diluted 1:300, anti-TDP43 (Proteintech, 10782-2-AP) diluted 1:200, in 1% goat serum/PBS, overnight at 4°C. Anti-p62/SQSTM1 (Santa Cruz Biotechnology, sc-28359) and anti-ubiquitin DAKO (Labome, Z0458) were gently

provided by Serena Carra and were used 1:100 in blocking solution 3% BSA and 0.2% Triton X-100. After extensive washing, cells were labelled with secondary antibodies: Goat anti-Mouse 488 (Invitrogen, A-11001), Goat anti-rabbit 488 (Invitrogen, A-11008), Donkey anti-mouse 647 (Invitrogen, A32787), Donkey anti-Rabbit 647 (Invitrogen, A32795) diluted 1:300 in 1% goat serum/1% donkey serum/ PBS for 45 minutes at room temperature. Lastly, the nuclei were counterstained with DAPI solution (1 μg/mL/PBS; Sigma-Aldrich, D9542) for 5 minutes at room temperature and then the coverslips were mounted using ProLong Diamond Antifade Mountant (Thermo Fisher Scientific, P-36961).

Confocal microscopy

Samples were imaged using an inverted confocal Olympus IX73 microscope equipped with a Crestoptics X-LIGHT V3 spinning disk system and a Prime BSI Express Scientific CMOS camera, and using an Olympus iX83 FluoView1200 laser scanning confocal microscope. The images were acquired using a LUCPlanFLN 20X objective (NA 0.45), a UPLANSApo 60X (NA 1.35) oil objective and a UPlanSApo 100X (NA 1.40) oil objective and were collected with the MetaMorph software (Molecular Devices).

The Z-stack confocal microscopy images were taken automatically (200 nm Z-spacing) and merged with the maximum intensity projection method. All images were processed with Laplacian of Gaussian filter (Ballarino et al., 2018) and intensity threshold, contrast and brightness were adjusted using the imageJ software. The co-planarity evaluation of the signals was performed combining the fluorescence distributions of each channel, recorded in the main grayscale value (expressed as arbitrary units), along Z-planes obtained from the imageJ Plot Z-axis profile plugin.

Imaging analyses

Colocalization signals were only considered if the profiles overlapped. The 3D-rendering of colocalized signals was performed with the imageJ software (Schneider et al., 2012) by using the 3D viewer. For the topological signal distribution analyses the same approach was applied: signals in co-planarity or in proximity were defined by the signal peak overlap along the X, Y and Z axes. In order to count circ-Hdgfrp3 signals, the ImageJ tool 'Analyse particle' was used while the specific circ-Hdgfrp3 localization in neurites was performed manually. The amount of colocalization between circ-Hdgfrp3, FUS-P517L and p62/SQSTM1 was quantified by 3D Pearson's correlation coefficients on Z-stacks using "JACoP" Fiji plugin (Bolte and Cordelières, 2006). In particular, after applying proper thresholding on whole image, a fixed ROI 3.53 x 3.45 μm was outlined in order to confine single circ-Hdgfrp3 spots surrounded with FUS-P517L signals and then JACoP plugin was launched. On the basis of classic concept, we define as "colocalized" signals with a Pearson's coefficient r>0 (positive correlation), and as "non-colocalized" signals with a Pearson's coefficient r < 0 (absolute anticorrelation).

RNA extraction and analyses

Total RNA was extracted using the Direct-zol Miniprep RNA Purification Kit (Zymo Research) with a 15-min on-column DNase treatment, according to the manufacturer's instructions.

RNA was reverse-transcribed using the PrimeScriptTM RT Reagent Kit (Takara Bio), according to the manufacturer's instructions. cDNA samples were analyzed by quantitative real time PCR using PowerUp SYBR Green Master Mix (Thermo Fisher Scientific), according to the manufacturer's protocol. RNA levels are relative to ATP5O mRNA, used as a control gene. Relative RNA quantity was calculated as the fold change (2^{-DDCt}) with respect to the control sample set as 1, unless differently specified. Oligonucleotides used for qRT-PCR are provided in Table S2. DNA amplification was monitored with an ABI 7500 Fast qPCR instrument. Data analysis was performed using the SDS Applied Biosystem 7500 Fast Real-Time PCR system software.

QUANTIFICATION AND STATISTICAL ANALYSIS

The standard deviation or standard error mean of data shown in the figures of this work, the statistical tests used to calculate significant differences, the exact value of N (number of biological replicates of the experiments), and the scale bar of the images are denoted in figure legends.

Significance values were depicted in the figures using the following key legend: *: p < 0.05, **: p < 0.01, ***: p < 0.001, ****: p < 0.0001. Error bars indicate SEM. GraphPad Prism was used for statistical test calculation.